We are IntechOpen, the world's leading publisher of Open Access books Built by scientists, for scientists

4,800
Open access books available

122,000
International authors and editors

135M
Downloads

Our authors are among the

154
Countries delivered to

TOP 1%
most cited scientists

12.2%
Contributors from top 500 universities

WEB OF SCIENCE™

Selection of our books indexed in the Book Citation Index in Web of Science™ Core Collection (BKCI)

Interested in publishing with us?
Contact book.department@intechopen.com

Numbers displayed above are based on latest data collected.
For more information visit www.intechopen.com

Chapter 2

Induced Force Hovering of Spherical Robot by Under-Actuated Control of Dual Rotor

G. Santos-Medina, K.Y. Heras-Gaytán, E.A. Martínez-García, R. Torres-Córdoba and V. Carrillo-Saucedo

Additional information is available at the end of the chapter

http://dx.doi.org/10.5772/63548

Abstract

This chapter discusses the design and modelling of a spherical flying robot. The main objective is to control its hovering and omnidirectional mobility by controlling the air mass differential pressure between two asynchronous coaxial rotors that are aligned collinearly. The spherical robot design has embedded a gyroscopic mechanism of three rings that allow the rotors' under-actuated mobility with 3DOF. The main objective of this study is to maintain the thrust force with nearly vertical direction. The change in pressure between rotors allows to vary the rotors' tilt and pitch. The system uses special design propellers to improve the laminar air mass flux. A nonlinear fitting model automatically calibrates the rotors' angular speed as a function of digital values. This model is the functional form that represents the reference input to control the rotors' speed, validated by three types controllers: P, PI, and PID. The robot's thrust and induced forces and flight mechanics are proposed and analysed. The simulation results show the feasibility of the approach.

Keywords: flight mechanics, flying control, robot modelling, thrust force, UAV, under-actuation

1. Introduction

Nowadays, unmanned aerial vehicle (UAV) robots are being deployed at an increased rate for numerous applications falling into a variety of engineering fields. There exist numer-

INTECH
open science | open minds

© 2016 The Author(s). Licensee InTech. This chapter is distributed under the terms of the Creative Commons Attribution License (http://creativecommons.org/licenses/by/3.0), which permits unrestricted use, distribution, and reproduction in any medium, provided the original work is properly cited.

ous kinds of rotary-wing-based robotic technologies in particular with active devices. Robots with rotating wings are capable to self-control over lift, propulsion, landing, hovering And take-off tasks [1–4]. Overcoming vertical flight (with minimum energy cost) is fundamental to accomplish autonomous precise tasks. One fundamental aspect in controlling and designing rotary-wing-based intelligent machines is to consider under-actuated issues to reduce the number of actuators. Under-actuated flying robots perform motion tasks more naturally, taking advantage of the inertial and gravitational forces, consequently, reducing the use of electrical energy. Biological flying birds are instances of extremely efficient under-actuated bodies. Therefore, in order to design flying machines with a reduced number of actuators, it is essential to model and understand the mechanical nature of the robot mechanics, the fluids and their physics-based relationship.

The present work has foundations on the prototype of a home-made spherical aerial robot. Some experiments can be viewed at https://www.youtube.com/watch?v=rrGH1Oh_beM. Nevertheless, the purpose of this chapter is not on showing and discussing experimental results, but on mathematically sustaining the hypothesis of the robot's flight mechanics and control. Unlike, known spherical design approaches [5–7], rather than deploying aileron-like propellers, we proposed yaw, pitch and roll changes through under-actuation exerting an inner gyroscopic mechanism. In the present chapter, the authors are particularly interested in disclosing the physical model of a dual rotary-wing spherical robot with an under-actuated gyroscopic mechanism. The model has been divided into four major areas: the robot's flight mechanics with direct and inverse solution, the thrusting or induced force model, the rotors control model and a proportional integral derivative (PID) based control with non-stationary reference values.

This chapter is organised as follows. In Section 2, the design and mechanical aspects of the aerial robot are presented. Section 3 presents the kinematic direct and inverse solutions of the flight mechanics. In Section 4, the acceleration components and forces involved in the robot's aerodynamics are discussed. Section 5 presents the robot's thrusting force model that involves two collinear induced forces. Section 6 presents the rotors' actuator speed models that are proposed from empirical measurements, and subsequently, the analytical solution is obtained. In Section 7, the actuators' feedback linear control is described. Finally, in Section 8, conclusions are drawn.

2. Spherical gyroscopic robot

Unlike other reported approaches [8–13], in this study, the authors have proposed an omnidirectional spherical design with two rotors vertically collinear (see **Figure 1**, right, and **Figure 2**).

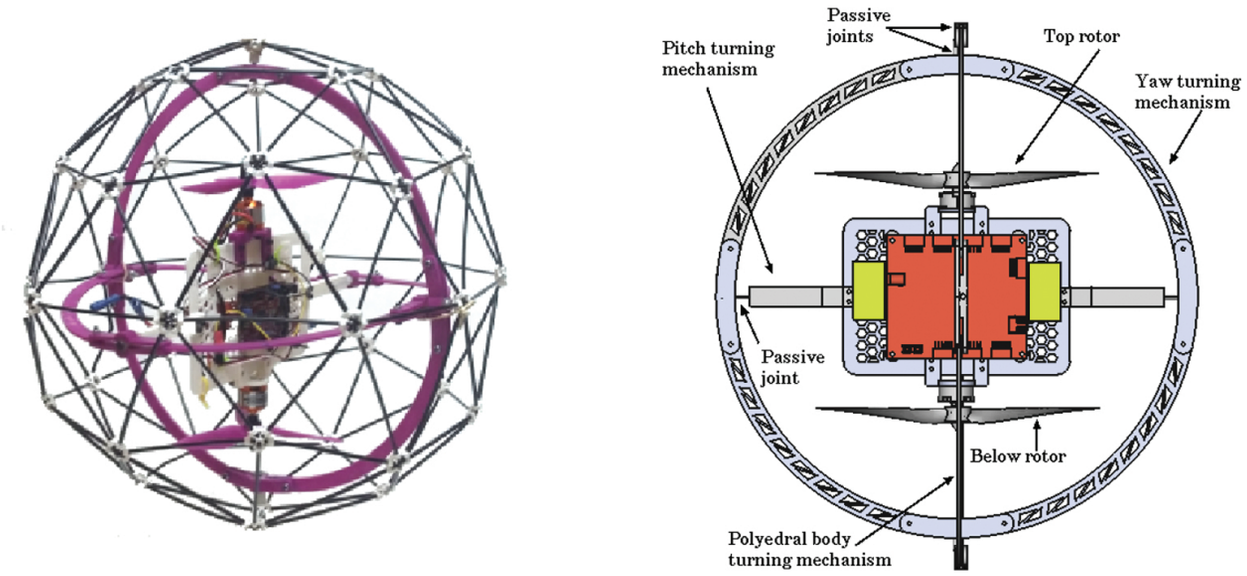

Figure 1. Left: Aerial robot real prototype. Right: Robot's main actuated and under-actuated mechanical elements.

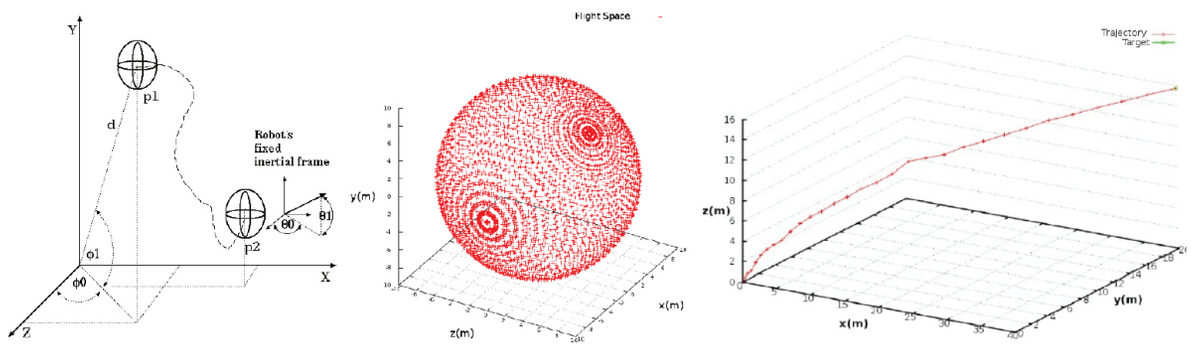

Figure 2. Left: Robot's global and local spherical coordinates. Centre: Robot's flying space (Eqs. (1)–(3)). Right: recursive trajectory generation (Texto) and (Texto).

3. Flight mechanics model

Flight mechanics refers to the study of geometry of flight of a heavier-than-air aircraft, considering aerodynamic aspects. Expressions (1)–(3) model the three-dimension robot's Cartesian kinematic components that describe its motion. The components, namely, x, y and z, are the space positions w.r.t. the location of the robot's starting flight. The proposed kinematic model is constrained with initial posture as the inertial frame origin, where d is the distance between the robot's instantaneous 3D position and its Cartesian origin. Azimuth angle ϕ_0 is w.r.t. the plane XY, and the elevation angle ϕ_1 is w.r.t. the Y-axis:

$$x = d\cos(\phi_1)\sin(\phi_0) \tag{1}$$

The y component (vertical) is expressed as

$$y = d\sin(\phi_1) \tag{2}$$

And, the z component is expressed as

$$z = d\cos(\phi_1)\cos(\phi_0) \tag{3}$$

For further purpose, the inverse solution is obtained by an algebraic arrangement of derivatives. The first-order derivatives of Eqs. (1)–(3) are obtained and shown in Eqs.(4)–(6),

$$\dot{x} = \dot{d}\cos(\phi_1)\sin(\phi_0) + d\cos(\phi_1)\cos(\phi_0)\dot{\phi}_0 - d\sin(\phi_1)\sin(\phi_0)\dot{\phi}_1 \tag{4}$$

The vertical component is expressed as

$$\dot{y} = \dot{d}\sin(\phi_1) + d\cos(\phi_1)\dot{\varphi}_1 \tag{5}$$

And, the z component is expressed as

$$\dot{z} = \dot{d}\cos(\phi_1)\cos(\phi_0) + d\cos(\phi_1)\cos(\phi_0)\dot{\phi}_0 \tag{6}$$

Figure 2 centre depicts the robot's flying space, which is spherical with the Cartesian origin at robot's starting flying task.

Expressing in the matrix form, the first-order derivative $d\mathbf{p}/dt$ w.r.t. time is

$$\dot{p} = \begin{pmatrix} \dot{x} \\ \dot{y} \\ \dot{z} \end{pmatrix} = \begin{pmatrix} dC_1C_0 & -dS_1S_0 & C_1S_0 \\ 0 & dC_1 & S_1 \\ -dC_1C_0 & -dS_1C_0 & C_1C_0 \end{pmatrix} \cdot \begin{pmatrix} \dot{\phi}_0 \\ \dot{\phi}_1 \\ \dot{d} \end{pmatrix} \tag{7}$$

By simplifying, the linear equation of direct kinematic is denoted by the Jacobian matrix **J** and the first-order vector of independent variables,

$$\dot{p} = J\dot{\Phi} \tag{8}$$

In order to obtain a recursive functional form equivalent to previous state variables, the derivatives are expressed in the following manner:

$$\frac{d}{dt}p = J\frac{d}{dt}\Phi \tag{9}$$

Time differentials are eliminated, and the integration operators complete the remaining differentials dp and $d\phi$:

$$\int_{\dot{p}_1}^{\dot{p}_2} dp = J\int_{\dot{\phi}_1}^{\dot{\phi}_2} d\Phi \tag{10}$$

Thus, to solve for the robot's Cartesian position a recursive form is obtained by algebraically reordering. Next, robot's position $\mathbf{p}_{t+1}$ is obtained by successive approximations of ϕ_t until ϕ_f:

$$p_{t+1} = p_t + J\left(\phi_f - \phi_t\right) \tag{11}$$

In addition, the kinematic inverse solution requires the inverse-squared Jacobian matrix, assuming that it is an invertible and non-singular matrix, with non-zero determinant:

$$J^{-1} = \frac{1}{d^2 C_1\left(\left[C_1 C_0\right]^2 + \left[S_0 S_1\right]\right)}\begin{pmatrix} dC_0 & 0 & -dS_0 \\ dC_1 S_0 S_1 & dC_1^2 & -dC_1 C_0 S_1 \\ \left(dC_1\right)^2 S_0 & -dC_1 C_0 S_1 & \left(dC_1\right)^2 C_0 \end{pmatrix} \tag{12}$$

Therefore, the first-order inverse kinematic is obtained by an algebraic approach:

$$\dot{\Phi} = J^{-1}\dot{p} \tag{13}$$

As described earlier, we complete the differentials dp and $d\phi$:

$$\int_{\dot{\Phi}_1}^{\dot{\Phi}_2} d\Phi = J^{-1}\int_{\dot{p}_1}^{\dot{p}_2} dp \tag{14}$$

By integrating both sides of the equality, respectively, a recursive inverse solution in terms of the rotor's angular speed is obtained,

$$\dot{\Phi}_{t+1} = \dot{\Phi}_t + J^{-1}\left(\dot{p}_f - \dot{p}_t\right) \tag{15}$$

where $\mathbf{p}_t$ is the actual robot 3D position and $\mathbf{p}_f$ represents the final desired position in space. To achieve such location, the robot recursively approximates the next desired rotor's controlled velocity. The next figure depicts a simulation result where the aerial robot successively approached the final desired position, staring from the Cartesian origin.

4. Aerodynamic robot's model

The aerodynamic robot's model refers to the application of the Newton's second law of motion in three dimensions to infer the thrusting force T and other involved forces that produce the Cartesian accelerations:

$$\begin{aligned}\ddot{x} = {} & \ddot{d}\,c_1 s_0 - \dot{d}s_1 s_0\dot{\phi}_1 + \dot{d}c_1 c_0\dot{\phi}_0 + \dot{d}c_1 c_0\phi_1 - ds_1 c_0\dot{\phi}_0\dot{\phi}_1 - dc_1 c_0\dot{\phi}_0^2 \\ & -dc_1 c_0\,\ddot{\phi}_0 - \dot{d}s_1 s_0\dot{\phi}_1 - dc_1 s_0\dot{\phi}_1^2 - ds_1 c_0\dot{\phi}_1\dot{\phi}_0 - ds_1 s_0\,\ddot{\phi}_1\end{aligned} \tag{16}$$

$$\ddot{y} = \ddot{d}\,s_1 + dc_1\dot{\phi}_1 + \dot{d}\,c_1\phi_1 - ds_1\dot{\phi}_1^2 + dc_1\ddot{\phi}_1 \tag{17}$$

$$\begin{aligned}\ddot{z} = {} & \ddot{d}\,c_1 c_0 - \dot{d}s_1 c_0\dot{\phi}_1 - \dot{d}c_1 s_0\dot{\phi}_0 - ds_1 c_0\phi_1 - dc_1 c_0\dot{\phi}_1^2 + ds_1 s_0\dot{\phi}_0\dot{\phi}_1 \\ & -ds_1 c_0\,\ddot{\phi}_1 - \dot{d}c_1 s_0\dot{\phi}_0 + \dot{d}s_1 s_0\dot{\phi}_0\dot{\phi}_1 - dc_1 c_0\dot{\phi}_0^2 - dc_1 s_0\,\ddot{\phi}_0\end{aligned} \tag{18}$$

In the matrix form, the following equation represents the direct kinematic solution for the Cartesian accelerations:

$$\ddot{p} = \begin{pmatrix} dc_1c_0 & -ds_1s_0 & c_1s_0 \\ 0 & dc_1 & s_1 \\ -dc_1c_0 & -ds_1c_0 & c_1s_0 \end{pmatrix}\begin{pmatrix} \dot{\phi}_0 \\ \dot{\phi}_1 \\ \dot{d} \end{pmatrix} + \begin{pmatrix} -dc_1c_0 & -dc_1c_0 & -2dc_1c_0 & 2dc_1c_0 & -2ds_1s_0 \\ 0 & -ds_1 & 0 & 0 & 2c_1 \\ -dc_1c_0 & -dc_1c_0 & -2ds_1s_0 & 2dc_1s_0 & -2ds_1c_0 \end{pmatrix} \tag{19}$$

or

$$\ddot{p} = J_1 \cdot \dot{\Phi} + J_2 \cdot \dot{\Phi}$$

From the previous expression, the vector acceleration is substituted into the Newton's second law of motion,

$$f = m \cdot \ddot{p} \tag{20}$$

where the Cartesian force components defined in robot's local inertial frame are expressed as follows:

$$f_x = T\cos(\theta_1)\sin(\theta_0) \tag{21}$$

The force component along the robot's local y component is expressed as

$$f_y = T\sin(\theta_1) \tag{22}$$

And, the force component along the robot's local Z component is expressed as

$$f_z = T\cos(\theta_1)\cos(\theta_0) \tag{23}$$

By simplifying the Cartesian force components in the matrix form

$$f = T\begin{pmatrix} c_1 s_0 \\ s_1 \\ c_1 c_0 \end{pmatrix} \tag{24}$$

And, by substituting the functional form of the vector force $\boldsymbol{f}$ into the Newton's second law,

$$m \cdot \ddot{p} = T\begin{pmatrix} c_1 s_0 \\ s_1 \\ c_1 c_0 \end{pmatrix} \tag{25}$$

Thus, by reordering the previous equation, we substitute the vector constraints $\mathbf{w}^T = (C_1S_0, S_1, C_1C_0)$. The acceleration vector $d^2\mathbf{p}/dt^2$ is a function of the next position $\mathbf{p}_{t+1}$ and the rotors variables:

$$Tw = m\,\ddot{p}\left(p_{t+1}, \Phi_f, \dot{\Phi}_t\right) \tag{26}$$

By dropping off the induced robot's force T,

$$T = w^{-1} m\,\ddot{p}\left(p_{t+1}, \Phi_f, \dot{\Phi}_t\right) \tag{27}$$

So far, in this expression, the total thrusting induced force T represents the robot's global flying force. Thus, T is an arithmetic result produced by the sum of the top rotor's induced force T_1 and the below rotor's induced force T_2 according to the following governing constraints:

(a) For $T_1 = T_2$, the inflow air mass is same throughout both rotors, hence $T = T_1 + T_2$.

(b) For $T_1 > T_2$, speed and air mass below rotor 1 are greater than rotor 2 inflow, $T = T_1 + \alpha_2 T_2$.

(c) For $T_1<T_2$, opposed to constraint (b), then $T_2 = \alpha_2 T_1$ and $T = T_1(1+\alpha_2)$.

Here, the numerical factors $\alpha_{1,2}$ are gains denoting rotors' speed-rate differences. For either constraint (b) or (c), the gyroscopic mechanism angles' tilt and pitch are affected, consequently changing the robot's azimuth and elevation angles.

5. Induced force model

According to the depictions of **Figure 3**, the rotors are continuously pushing the air down. As per Newton's third law, an equal and opposite reaction force, denoted as rotor thrust, is acting on the rotor due to air. The induced force model refers to the thrusting force exerted to accelerate the robot. And at a constant velocity the quasi-static hovering is achieved [1–4].

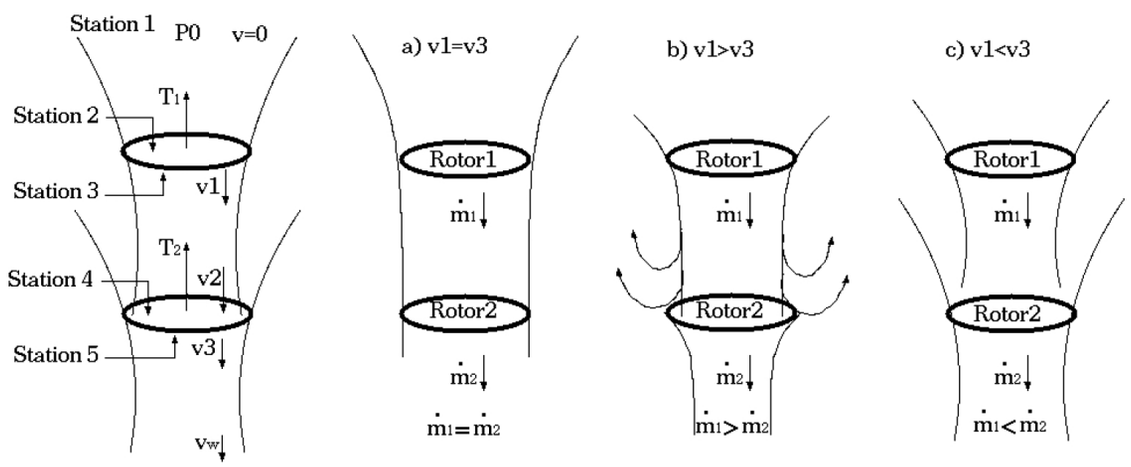

Figure 3. Rotors' flow conditions in the slip streams.

The momentum conservation is obtained by relating the induced force T_2 to the rate of momentum change. It is the mass rate and the far-field wake-induced velocity v_w below rotor 2, where $dm/dt=\varrho A v_2$ and the rotor disk area $A = \pi R^2$. Thus, the moment conservation

$$T = \dot{m} v_w \tag{28}$$

The energy conservation per unit time

$$Tv = \frac{1}{2}\dot{m} v_w^2 \tag{29}$$

To obtain a relationship between v and v_w, let us substitute T and dm/dt,

$$\dot{m} v_w v = \frac{1}{2}\dot{m} v_w^2 \tag{30}$$

Algebraically simplifying,

$$v = \frac{1}{2} v_w; v_w = 2v \tag{31}$$

Hence, substituting v_w into T,

$$T = \dot{m} v_w = 2\dot{m} v \tag{32}$$

Then,

$$T = 2\rho A v^2 \tag{33}$$

Dropping off v, the following expression is obtained;

$$v = \sqrt{\frac{T}{2\rho A}} \tag{34}$$

The propulsive power P_w is the thrusting force T capable to move the robot at a given velocity (distance over time):

$$P_w = Tv = T\sqrt{\frac{T}{2\rho A}} \tag{35}$$

The induced power per unit thrust for a hovering rotor can be written as

$$\frac{P_w}{T} = v = \sqrt{\frac{T}{2\rho A}} \tag{36}$$

The above expression indicates that, for a low inflow velocity, the efficiency is higher. This is possible if the rotor has a low disk loading (T/A). Note that the parameter determining the induced power is essentially $T/(A)$. Therefore, the effective disk loading increases with an increase in altitude and temperature.

From previous analysis, let us now precisely define the thrusting force for rotors 1 and 2, according to **Figure 3** (left side). For rotor 1, the air mass flow is

$$\dot{m}_1 = \rho A_1 v_1 \tag{37}$$

Hence, considering only rotor 1, the induced force is

$$T_1 = \dot{m}_1 v_2 \tag{38}$$

The energy conservation principle for rotor 1 is expressed as

$$T_1 v_1 = \frac{1}{2}\dot{m}_1 v_2^2 \tag{39}$$

And finding a relationship between v_1 and v_2 in accordance with **Figure 3** (left side),

$$v_2 = 2v_1 \tag{40}$$

Thus,

$$T_1 = 2\rho_1 A_1 v_1^2 \tag{41}$$

The induced air velocity induced by rotor 1 is modelled by

$$v_1 = \sqrt{\frac{T_1}{2\rho_1 A_1}} \tag{42}$$

Similarly, modelling both the induced force T_2 and velocity v_2 for rotor 2, the following analysis is developed. The airflow rate,

$$\dot{m}_2 = \rho_2 A_2 v_3 \tag{43}$$

And the induced force T_2 considers the inflow air mass and the far-field wake-induced velocity v_w,

$$T_2 = \dot{m}_2 v_w \tag{44}$$

The energy conservation for the second rotor is expressed as

$$T_2 v_3 = \frac{1}{2}\dot{m}_2 v_w^2 \tag{45}$$

The relationship between far-field wake-induced air velocity v_w and v_3 is given by v_w=2v_3, and

$$T_2 = 2\rho_2 A_2 v_3^2 \tag{46}$$

Therefore, the second rotor's air induced velocity is

$$v_3 = \sqrt{\frac{T_2}{2\rho_2 A_2}} \tag{47}$$

From the three previous postulates of **Figure 3**, let us deduce the conditions when both rotors, although asynchronous, simultaneously induce the airflow equally, when v_1=v_3 (**Figure 3a**). For this case, the total robot's thrusting force T=T_1+T_2,

$$T = 2\rho_1 A_1 v_1^2 + 2\rho_2 A_2 v_3^2 \tag{48}$$

For case 1, let us assume A_1=A_2 and v_2=v_3 through the second rotor's disc area. And,

$$v_w = 2v_3; likewise, v_2 = 2v_1; hence v_w = 2(2v_1) = 4v_1 \tag{49}$$

Rewriting total T as a function of v_1, thus we have

$$\rho_2 = \frac{m_c}{v_c} \tag{50}$$

The air mass variation is denoted as the mass derivative w.r.t. time,

$$\dot{m} = \rho_2 A V_2 \tag{51}$$

Now, for the case v_1>v_3,

$$T = T_1 + \alpha_2 T_2 \tag{52}$$

Let us substitute our T_1 and T_2 models previously analysed,

$$T = 2\rho_1 A_1 v_1^2 + 2\rho_2 A_2 v_3^2 \tag{53}$$

In addition, A_1=A_2, v_2=2v_1 and v_w=2v_3, but v_2>v_3 hence v_3=$\alpha_2 v_2$. Thus, v_w=2(α_2 2(2v_1)), and we obtain the relationship between the far-field wake-induced velocity and v_1:

$$v_w = 6\alpha_2 v_1 \tag{54}$$

By substituting v_1 into expression T, developing and factorising algebraically,

$$T = 2Av_1^2\left(\rho_1 + 4\alpha_2\rho_2\right) \tag{55}$$

Similarly, for the case when v_1<v_3, T=T_1(1+α_2),

$$T = 2\rho_1 A_1 v_1^2 + 2\rho_2 A_2 v_3^2 \tag{56}$$

for this case, A_1=A_2, v_2=2v_1 and v_w=2v_3. However, just above and below rotor 2, v_2<v_3, and therefore v_2=$\alpha_2 v_3$, then v_3=2v_2/α_2.

$$T = 2\rho_1 A v_1^2 + 2\rho_2 A\left(2\frac{v_1}{\alpha_2}\right)^2 \tag{57}$$

Factorizing and algebraically arranging,

$$T = 2Av_1^2\left(\rho_1 + \frac{8\rho_2}{\alpha_2^2}\right) \tag{58}$$

Solving the parameter α_2 for each of the three cases,

$$\alpha_2^2 = \begin{cases} 4, & v_1 = v_3 \\ 1, & v_1 > v_3 \\ \sqrt{2}, & v1 < v_3 \end{cases} \tag{59}$$

Therefore, we synthesise the total thrusting force T for all cases by

$$T = 2Av_1^2\left(\rho_1 + \alpha_2^2\rho_2\right) \tag{60}$$

Therefore, from Eq. (60), now we have a functional form for the thrusting force T. Thus, to reach a controlled rotors' velocity, we must establish a relationship between the induced velocity v_1 and the rotor angular velocity $d\phi/dt$ using the tip speed of the rotor blade as reference. The rotor inflow is represented in non-dimensional form as

$$\lambda = \frac{v_3}{\dot{\phi}R} = \sqrt{\frac{C_T}{2}} \tag{61}$$

where C_T is the thrust coefficient modelled by

$$C_T = \frac{T}{\rho_2 A\left(\dot{\phi}_t R\right)^2} \tag{62}$$

Therefore, the following equality allow us to deduce C_T with more

$$\dot{\phi} = \frac{v_1}{R\sqrt{\frac{C_T}{2}}} \tag{63}$$

Thus, substituting (Texto) into v_1,

$$v_1 = \left(\dot{\phi} R \sqrt{\frac{C_T}{2}}\right)^2 \tag{64}$$

And subsequently, $v_1{}^2$ is substituted into T,

$$T = A\left(\dot{\phi}^2 R^2 C_T\right)(\rho_1 + \alpha_2^2 \rho_2) \tag{65}$$

Therefore, the induced force T arising from the fluid mechanics equation (65) is equated with the induced force of the flight mechanics equation (27), the following expression is obtained:

$$2A\left(\dot{\phi}^2 R^2 \frac{C_T}{2}\right)(\rho_1 + \alpha_2^2 \rho_2) = w^{-1} m\ddot{p} \tag{66}$$

Our objective is to find an analytical solution for the rotor speed required to reach the induced velocity v_1 and the induced force T, which is governed by the flight mechanics law. The induced air mass velocity v_1 can be expressed in terms of the rotor speed that is controlled to obtain the desired angular velocity,

$$\dot{\phi} = \sqrt{\frac{m w^{-1} \ddot{p}}{A R^2 C_T (\rho_1 + \alpha_2^2 \rho_2)}} \tag{67}$$

This model represents the independent variable to control the motors' Speed of Eq. (73) or Eq. (74):

Thus, it follows a set of empirical temperature measurements where some experimental hovering experiments were carried out. The plots in **Figure 4** depict how the air pressure is affected as the temperature varies over time.

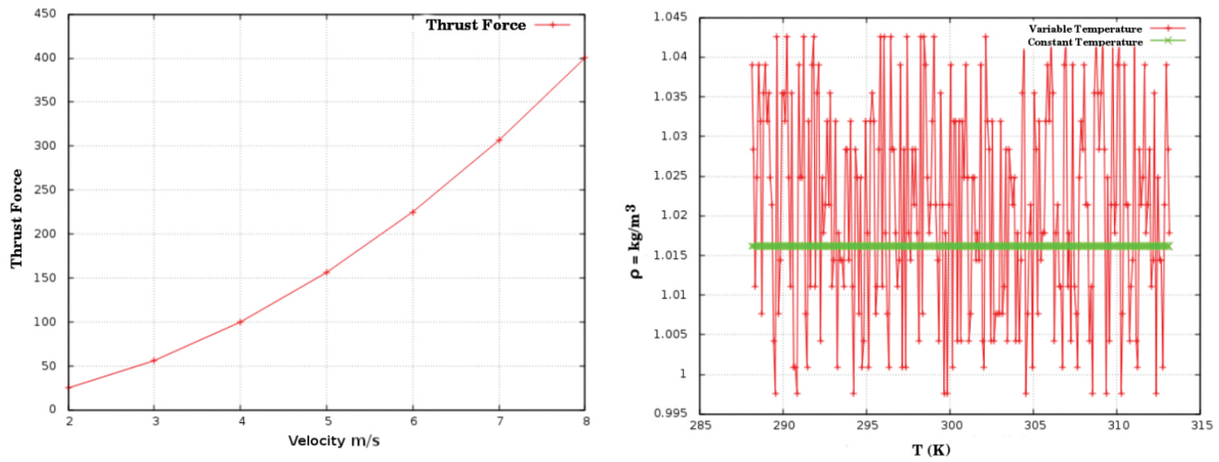

Figure 4. Left: Thrusting force w.r.t. induced velocity. Right: Air mass density as temperature varies.

6. Actuators' speed model

The actuators' self-calibration speed model is discussed in this section. The real rotary velocity in a range from minimal to maximal values approached a logarithmic model. It considered the empirical set of angular speed measurements w.r.t. digital controls. The inherent physical variations, such as temperature, air pressure, density and air dust particles, affected the actuators' performance. Since the angular speed value capable to hover the spherical robot's body is disturbed, a self-calibration is required to maintain position control as accurate as possible. From experiments, the empirical models that obtained (**Figure 5**) φ vs. *d* are fitted according to the next model. The parameters *A* and β are unknown and must fit the speed measurements φ, w.r.t to digital word *d*,

$$\dot{\phi} = A + \beta ln(d) \tag{68}$$

We temporally substitute *d'*=ln(d), and thus the rotary speed

$$\dot{\phi} = A = \beta d' \tag{69}$$

To estimate the unknown parameter β, a linear mean-squared method is applied,

$$\beta = \frac{n\left(\sum d'\dot{\phi} - (\sum d')(\sum \dot{\phi})\right)}{n(\sum d'^2) - (\sum d')^2} \tag{70}$$

Subsequently, the previous parameter solution is used in the next expression *A*,

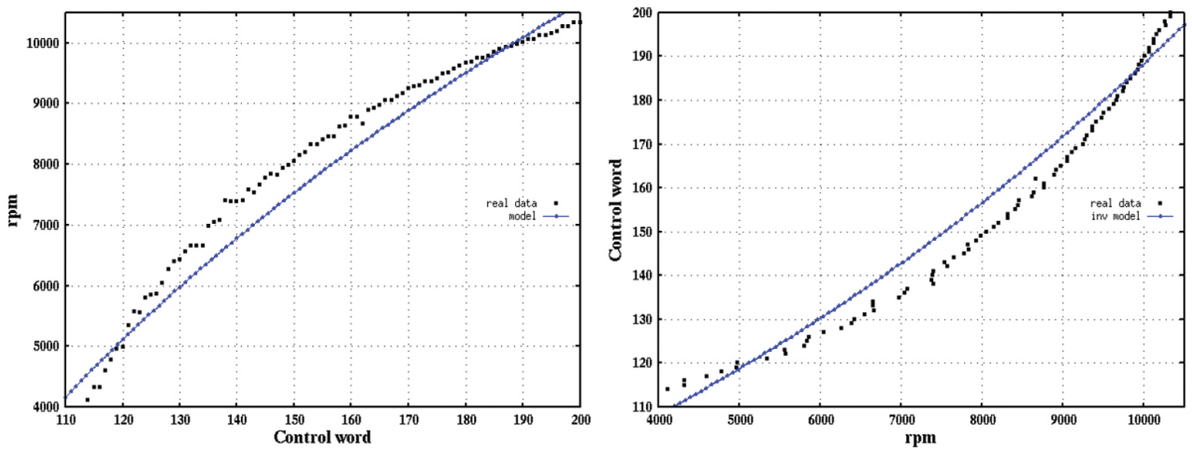

Figure 5. Actuator's raw measurements. Left: Direct solution. Right: Inverse solution.

$$A = \frac{\sum \dot{\phi}}{n} - \beta \frac{\sum d'}{n} \tag{71}$$

By substituting the parameters numerical values, the rotary speed model is obtained as follows:

$$\dot{\phi} = 10838.57637 ln(d) - 46776.63059 \tag{72}$$

In addition, in order to obtain the inverse solution, we algebraically drop off the variable d from Eq. (72),

$$d = e^{\frac{\dot{\phi} - A}{\beta}} \tag{73}$$

And numerical parametric values from Eq. (72) are substituted into (73) to obtain

$$d = e^{\frac{\dot{\phi} - 46776.6306}{10838.5764}} \tag{74}$$

In order to compare how our theoretical model fits the empirical model, both inverse and direct operation control modes are depicted in **Figure 5**.

7. Rotor's speed control

From the previous section, the actuators' speed model is now used to formulate a feedback linear control. Let us assume that a rotor control variable (i.e., angle, velocity and acceleration) should ideally be equal to the real sensed control variable, as expressed by the next equality (75). Nevertheless, in a realistic scenario real and ideal control variables are different due to a

number of factors, such as frictions, inertial and gravity forces, motor electromagnetic performance and so on. Thus, both variables are approached by a multiplicative gain or factor alpha, which approximates both numerical values according to the relation

$$\varphi = k\hat{\phi} \tag{75}$$

Assuming an arbitrary actual derivative order, the equation is equivalently expressed as

$$\frac{d}{dt}\varphi = k\frac{d}{dt}\phi \tag{76}$$

The time differentials are eliminated and the remaining differentials are obtained by solving the following definite integrals,

$$\int_{\varphi_1}^{\varphi_2} d\,\varphi = k\int_{\phi_1}^{\phi_2} d\,\phi \tag{77}$$

By solving the definite integrals,

$$\varphi_2 - \varphi_1 = k(\phi_2 - \phi_1) \tag{78}$$

In this case, $\hat{\varphi}_2$ is the expected or the reference value to be reached ideally, $\hat{\varphi}_2 = \varphi^{\text{ref}}$. Thus, by adjusting the times sub-interval labels, and algebraically reordering, the next recursive numerical successive approximation equation is expressed as follows:

$$\varphi_{t+1} = \varphi_t + k\left(\varphi^{ref} - \phi_t\right) = \varphi_t + ke_t \tag{79}$$

From the previous expression, the error ke_t is spanned into the past (angular displacement), the actual (rotary speed) and the future (angular accelerations) errors in order to cover the whole error history. And the general constant gain k is proportional to k_p, k_I and k_d. Thus,

$$\varphi_{t+1} = \varphi_t + \left(k_p e_p + k_I e_I + k_d e_d\right) \tag{80}$$

Therefore, the next feedback proportional error e_p (rad/s) with proportional gain k_p (dimensionless) is obtained with the observation ϕ_t measured online. And the reference model (Texto) is established in terms of the instantaneous control word δ_t:

$$k_p e_p = k_p\left(\dot{\phi}^{ref} - \dot{\phi}_t\right) = k_p\left(aln(\delta) - b - \dot{\phi}_t\right) \tag{81}$$

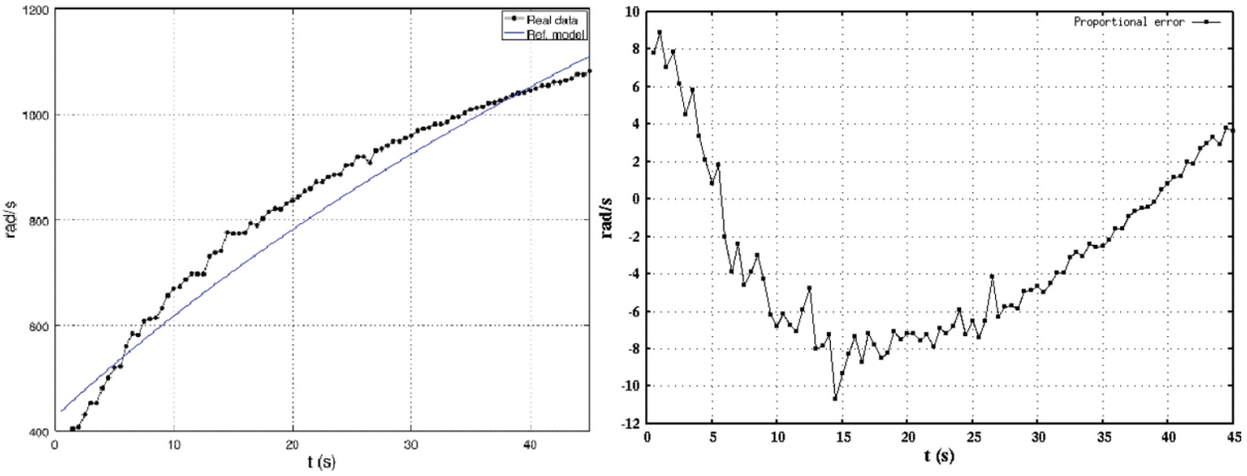

Figure 6. Left: Measurement and reference proportional models. Right: Proportional error.

For illustrative purpose, an accelerative rotor's task to exert robot's propulsion was performed. **Figure 6** (left) depicts both the reference model ϕ^{ref} and the observation $\phi(t)$.

In addition, **Figure 6** (right) shows the proportional error behaviour ϕ^{ref}-$\phi(t)$ without k_p. Furthermore, the feedback integral error e_I (rad/s) with integral gain k_I (dimensionless) is expressed by the time integration of the difference of $(d^2\phi/dt^2 - d^2\phi(t)/dt^2)$.

$$k_I e_I = k_I \left(\int \left(\ddot{\phi}^{ref} - \ddot{\phi}_t \right) dt \right) \tag{82}$$

The observation model $d^2\phi/dt^2$ was obtained online by the numerical derivatives of the optical encoder according to the following relationship:

$$\ddot{\phi}(t) = \frac{\dot{\phi}_{t_2} - \dot{\phi}_{t_1}}{t_2 - t_1} \tag{83}$$

In addition, since the observation model inherently poses perturbations, an analytical reference model $d^2\phi^{ref}/dt^2$ was obtained using a nonlinear regressive fitting process for parameters identification,

$$\begin{pmatrix} \sum \ddot{\phi}_i \\ \sum \ddot{\phi}\, t_i \\ \sum \ddot{\phi}_i\, t_i^2 \end{pmatrix} = \begin{pmatrix} n & \sum t_i & \sum t_i^2 \\ \sum t_i & \sum t_i^2 & \sum t_i^3 \\ \sum t_i^2 & \sum t_i^3 & \sum t_i^4 \end{pmatrix} \cdot \begin{pmatrix} a_0 \\ a_1 \\ a_2 \end{pmatrix} \tag{84}$$

where the previous expression is similarly expressed as

$$y = A \cdot x \tag{85}$$

And by solving vector **x**,

$$x = A^{-1} \cdot y \tag{86}$$

Hence, the reference model is a theoretical nonlinear function of time,

$$\ddot{\phi}^{ref}(t) = 34.7950 - 1.2832t + 0.0145t^2 \tag{87}$$

Therefore, for the sake of the integral control u_I (rad/s), the angular acceleration reference model (Texto) is substituted next in its general form:

$$u_I = k_I \left(\int (a_0 - a_{1t} + a_2 t^2) - \ddot{\phi}(t) dt \right) \tag{88}$$

Finally, in order to keep data homogeneity (numerical data subtraction), time integration is obtained by the trapezoid rule for numerical integration,

$$\begin{aligned} \dot{\phi}_k = \frac{t_f - t_0}{2n} \Big[\left(\ddot{\phi}_0^{ref} - \ddot{\phi}_0(t) \right) + 2 \sum \left(\ddot{\phi}_t^{ref} - \ddot{\phi}_t \right) \\ + \left(\ddot{\phi}_{t_f}^{ref}(t) - \ddot{\phi}_{t_f}(t) \right) \Big] \end{aligned} \tag{89}$$

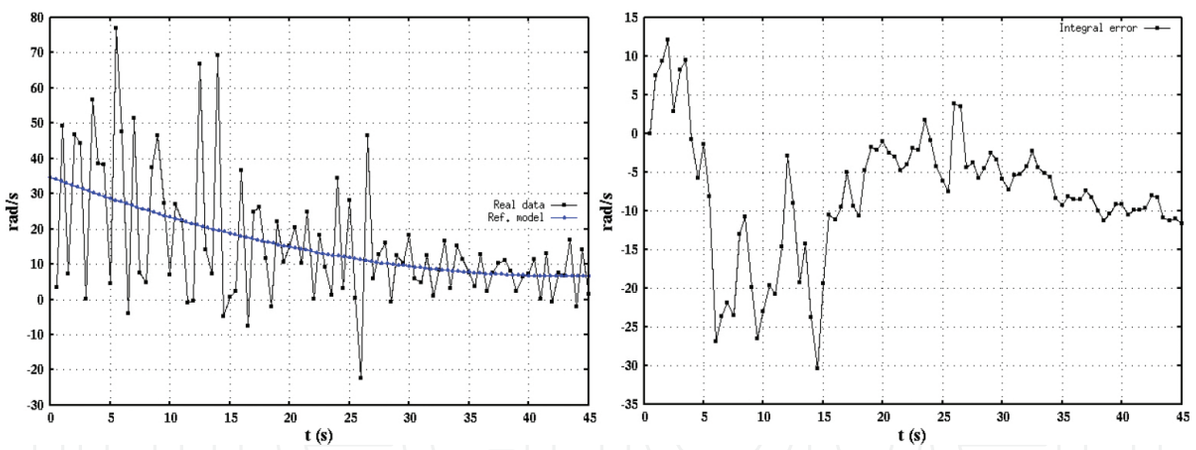

Figure 7. Left: Measurement and reference integral models. Right: Integral error.

Figure 7 (left) depicts both reference and empirical models integrated with time. **Figure 7** (right) shows the integral error behaviour.

In addition, the derivative control u_d=$k_d e_d$ (rad/s) with feedback derivative error e_d, and with derivative gain k_d (dimensionless), improves the closed-loop stability as follows:

$$k_d e_d = k_d \left(\frac{d}{dt} \phi^{\text{ref}} - \frac{d}{dt} \phi_t \right) \tag{90}$$

In order to obtain the time derivative observation model, the rotor's angle evolution $\phi(t)$ (rad) is observed online using an optical encoder during the time slot where velocity and acceleration are also measured. As the measurements are read with noise, the analytical reference model is fitted as a nonlinear polynomial of the following form:

$$\phi^{\text{ref}}(t) = -3709.6273 + 2116.9484t + 27.9289t^2 \tag{91}$$

where the derivative error general form is expressed as

$$k_d e_d = k_d \frac{d}{dt}\left(-b_0 + b_{1t} + b_2 t^2 - \phi(t)\right) \tag{92}$$

Figure 8 (left) depicts both reference $\phi^{\text{ref}}(t)$ and observation $\phi(t)$ models together. Although both curves are apparently fitted, the vertical scale is provided in thousands of radians. **Figure 8** (right) shows the derivative error scale.

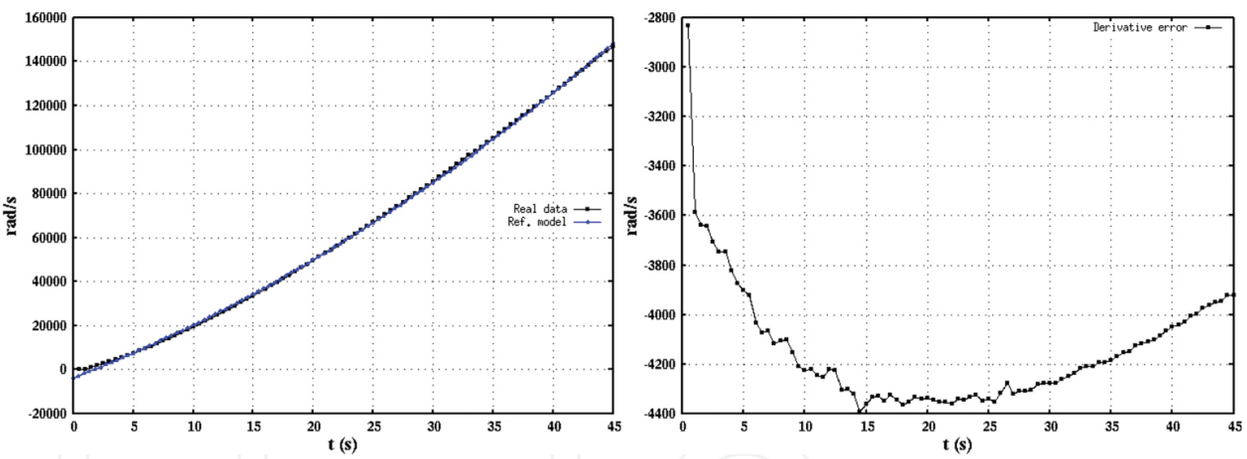

Figure 8. Left: Measurement and reference derivative models. Right: Derivative error.

Generally, the PID controller is expressed by the next expression

$$\begin{aligned} u_t = k_p\left((aln(d) - b) - \dot{\phi}_i\right) + k_I\left(\int_t \left(a_0 - a_{1t} + a_{2t}^2 - \ddot{\phi}_t\right) dt\right) \\ + k_d\left(\frac{d}{dt}\left(-b_0 + b_{1t} + b_{2t}^2 - \phi(t)\right)\right) \end{aligned} \tag{93}$$

Therefore, the controlled rotor's velocity that is recursively calculated by $d\varphi_{t+1}/dt = d\varphi_t/dt + u_t$ is applied, and we established the following controller choices: proportional (P), proportional

integral (PI) and proportional-integral-derivative. **Figure 9** (left) depicts the rotors' angular speed without control and with three types of controllers. The constant parameters were adjusted accordingly to obtain such results. We can see that after 25 s the responses P and PI gradually converge w.r.t. the raw rotor's speed (**Figure 9**, left).

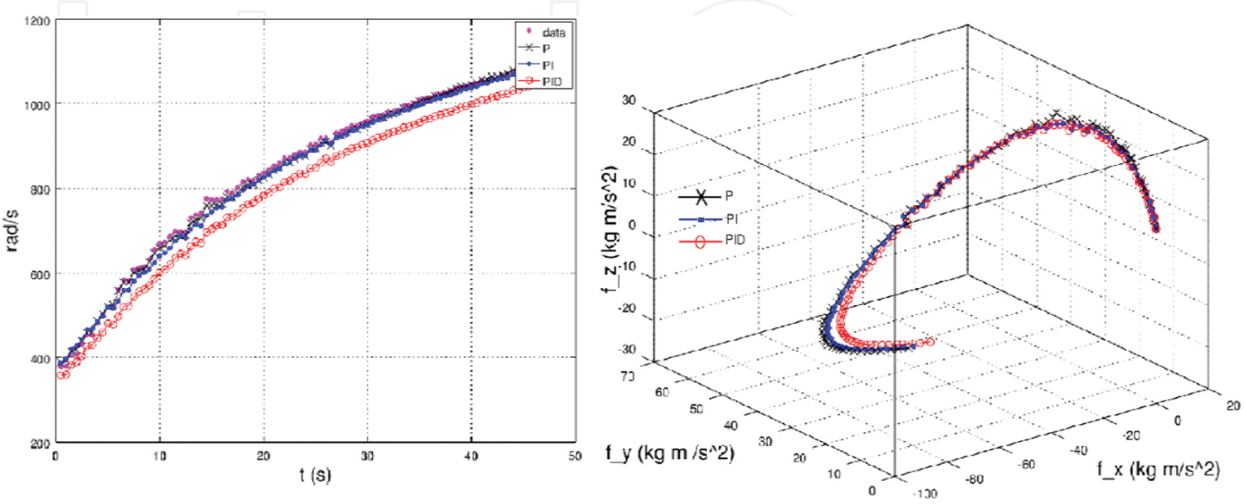

Figure 9. Controllers P, PI and PID. Left: Rotor's angular speed. Right: Induced Cartesian forces.

In addition, with the controlled rotor's speed output, the induced force is iteratively calculated by

$$T(\dot{\varphi}_{t+1}) = A\dot{\varphi}_{t+1}^2 R^2 C_T(\rho_1 + \alpha_2^2 \rho_2) \tag{94}$$

Thus, **Figure 9** (right) depicts the induced component forces that are produced using three types of controllers.

8. Conclusions

This work briefly introduced the design of an aerial spherical robot with under-actuated gyroscopic mechanism. Although the purpose of this study was not to describe the robot flying and physical capabilities, the main objective was to demonstrate the induced force model deploying dual collinear rotary wings with no steering actuators. This study describes the following four major areas: the robot flight mechanics, the model of the induced thrusting forces, the self-calibration actuators' Speed model validated with three types of controllers (P, PI, PID) to drive the rotors' motor speed. The proposed aerodynamic mechanism poses neither ailerons nor propellers for steering control. Although the platform is a home-made laboratory prototype with special arrangements, the main focus of this chapter is to model the hypothesis of controlling the robot's directions by varying rotors' asynchronous speed. To achieve this, the under-actuated gyroscopic mechanism provides the ability to control its inner yaw, pitch

and roll angles. Until this stage, the robot development is under an early control capability. However, this study presents mathematical solutions and simulation results to demonstrate the proposed aerodynamic hypothesis.

Author details

G. Santos-Medina, K.Y. Heras-Gaytán, E.A. Martínez-García*, R. Torres-Córdoba and V. Carrillo-Saucedo

*Address all correspondence to: edmartin@uacj.mx

Laboratorio de Robótica, Institute of Engineering and Technology, Universidad Autónoma de Ciudad Juárez Ave. Del Charro, Cd. Juarez, Chihuahua, Mexico

References

[1] Venkatesan C. Fundamentals of helicopter dynamics. CRC Press Taylor and Francis Group; 2015.

[2] Stepniewski W, Keys C. Rotary-wing aerodynamics. New York: Dover Publications; 1984.

[3] Johnson W. Helicopter theory. New York: Dover Publications; 1994.

[4] Seddon J, Newman S. Basic helicopter aerodynamics. Chichester, England: Wiley; 2011.

[5] Briod A, Kornatowski P, Zufferey J, Floreano DA. Collision-resilient flying robot. Journal of Field Robotics, 31(4), 496–509, 2013.

[6] Dudley C, A Spherical Aerial Terrestrial Robot, MSc Thesis, University of Nevada, Reno, 2014.

[7] Briod A, Klaptocz A, Zufferey J-C, Floreano D. The AirBurr: a flying robot that can exploit collisions. International Conference on Complex Medical Engineering, Japan, pp. 569–574, 2012.

[8] Alkalla MG, Fanni MA, Mohamed M.A novel propeller-type climbing robot for vessels inspection. IEEE International Conference on Advanced Intelligent Mechatronics, South Korea, pp.1623–1628, 2015.

[9] Mizutani S,Okada Y,Salaan CJ,Ishii T,Ohno K,Tadokoro S. Proposal and experimental validation of a design strategy for a UAV with a passive rotating spherical shell. IEEE/RSJ IROS, Germany, pp. 1271–1278, 2015.

[10] Czyba R, Szafranski G, Janik M, Pampuch K, Hecel M, Development of co-axial Y6-Rotor UAV—design, mathematical modeling, rapid prototyping and experimental

validation. International Conference on Unmanned Aircraft Systems, USA, pp. 1102–1111, 2015.

[11] Kawasaki K, Zhao M, Okada K, Inaba M. MUWA: multi-field universal wheel for air-land vehicle with quad variable-pitch propellers. IEEE/RSJ IROS, Japan, pp. 1880–1885, 2013.

[12] Ho-Joon L, Han-Woong A, Jae-Kwang L, Ju L, Sung-Hong W. Newly proposed hybrid type mutli-DOF operation motor for multi-copter UAV systems. IEEE Energy Conversion Congress and Exposition, Canada, pp. 2782–2790, 2015.

[13] Zhang W, Fan N, Wang Z, Wu Y, Modeling and aerodynamic analysis of a ducted-fan micro aerial vehicle. International Conference on Modelling, Identification & Control, China, pp. 768–773, 2012.

IntechOpen